Porous TiWO$_3$/SrWO$_4$ with high titanium molar ratio for efficient photoelectrocatalytic nitrogen reduction under mild conditions

Kaiyi Chen [a], Xiaohong Xu [a], Qiong Mei [a], Jingwei Huang [b], Guidong Yang [c], Qizhao Wang [a,b,*]

[a] School of Water and Environment, Key Laboratory of Subsurface Hydrology and Ecological Effects in Arid Region of Ministry of Education, Chang'an University, Xi'an 710054, Shaanxi, China
[b] College of Chemistry and Chemical Engineering, Northwest Normal University, Lanzhou 730070, Gansu, China
[c] School of Chemical Engineering and Technology, Xi'an Jiaotong University, Xi'an, Shaanxi 710049, China

ARTICLE INFO

ABSTRACT

Ammonia synthesized by nitrogen reduction is the most promising new energy material. Photoelectrocatalytic (PEC) nitrogen reduction reaction (NRR) occurs under ambient conditions and is the optimal alternative to the energy-intensive Haber-Bosch method. Here, we report the one-step reaction synthesis of Ti–WO$_3$/SrWO$_4$ as a photocathode for ammonia synthesis. First-principles calculations demonstrate that Ti doping can afford nitrogen-adsorption sites, and Ti^{3+} undergoes chemical adsorption and becomes a nitrogen-activation site by providing electrons to nitrogen. Under light irradiation, the photogenerated electrons are captured by Ti^{4+}; this is conducive to the activation and regeneration of Ti^{3+}, thus forming a nitrogen fixation cycle and improving the nitrogen fixation yield. At − 0.5 V vs. RHE, the ammonia synthesis efficiency reaches 11.17 μg h^{-1} cm^{-2}, which is four times that of SrWO$_4$. Furthermore, the high stability and N-gas sensitivity of Ti–WO$_3$/SrWO$_4$ in the NRR indicate that it can be used as an efficient and stable photoelectrocatalyst for ammonia synthesis.

1. Introduction

NH$_3$ is an important chemical raw material and intermediate in the fertilizers and the basic chemical industry [1–4]. Compared with hydrogen energy, it has the characteristics of easy storage and transportation and has high potential to be a source of clean energy [5–8]. The Haber--Bosch method developed in the early 19th century is the most widely used nitrogen reduction reaction in industry; however, it consumes a considerable amount of energy and releases extremely polluting gases into the environment [9–11]. In 1977, Schrauzer and Guth proved that TiO$_2$ has photocatalytic nitrogen reduction activity in the presence of water and nitrogen. Many researchers have carried out a series of modification on TiO$_2$ to improve the effect of photocatalytic nitrogen reduction to ammonia. However, photocatalytic materials cannot achieve a solar-energy conversion efficiency of 5–10 %. Photoelectrocatalytic (PEC) nitrogen reduction reaction (NRR) for NH$_3$ synthesis is considered a high-potential alternative method to achieve this aim [12–14]. In this reaction, nitrogen and water are used as materials to convert solar energy to chemical energy by producing NH$_3$ under bias voltage and mild conditions. The reaction has a low yield;

hence, there is an urgent requirement to develop an efficient and environmentally friendly NRR photoelectrocatalyst and reaction system. The energy band structure is the primary factor affecting the performance of semiconductor materials, and it determines the possibility of photocatalytic redox reactions [15–18].

To improve the efficiency of nitrogen reduction, researchers explored many semiconductors, such as g-C$_3$N$_4$ [19–21], TiO$_2$ [22–25], tungsten oxide compounds [26–29], and molybdenum compounds [30–32], for photocatalytic or PEC NH$_3$ synthesis. Among them, SrWO$_4$ is a wide bandgap semiconductor that has been popular for photocatalysis. Fe-doped SrWO$_4$ nanoparticles, which have a wider light absorption range and less charge recombination than pure SrWO$_4$ nanoparticles, exhibit higher photocatalytic nitrogen fixation performance [33]. The rate of NH$_3$ production from WO$_3$ with controlled oxygen vacancies prepared by the hydrogen pressure re-calcined process was 150 μmol g$_{cat}^{-1}$ h^{-1}, which was about four times higher than that of the original WO$_3$ [34,35]. WO$_3$ can modulate the surface oxygen vacancies by changing the annealing atmosphere (air, CO, H$_2$, or Ar), thereby regulating N$_2$ adsorption on the surface and improving the electrocatalytic efficiency of NH$_3$ synthesis. The NH$_3$ yield was about 4.2 μg h^{-1}

mg_{cat}^{-1} after heat treatment in H_2 at 300 °C.

However, few studies explored the regulation of WO_3 and $SrWO_4$ bands. In this study, $SrWO_4$ and WO_3 were combined to form a heterojunction, and this heterojunction was doped with Ti to develop a PEC system of the Ti–WO_3/$SrWO_4$ photocathode. The excellent electronic transition ability of $SrWO_4$ was combined with the narrow band gap of WO_3 to impart complementary advantages to the heterojunction, thereby expanding the visible light absorption range and enhancing electron transmission. The PEC NRR-based NH_3 synthesis system requires six electrons and six holes to complete a nitrogen fixation cycle. The doped Ti can activate the electron–hole cyclic transport. The six electrons transmitted from $SrWO_4$ and WO_3 to Ti and the H^+ in the solution cause NH_3 generation. The equation for the reaction is shown in Eq. (1).

$$N_{2(g)} + 8H^+_{(aq.)}(or6H^+_{(aq.)}) + 6e^- \leftrightarrow 2NH^+_{4(aq.)}(or2NH_{3(g)}) \tag{1}$$

2. Experimental

2.1. Materials

Sodium tungstate ($NaWO_4 \cdot 2H_2O$), ammonium oxalate ((NH_4)$_2C_2O_4$), strontium nitrate ($Sr(NO_3)_2$), tetrabutyl titanates ($C_{16}H_{36}O_4Ti$), sodium citrate ($Na_3C_6H_5O_7$), sulfuric acid (H_2SO_4), hydrochloric acid (HCl), sodium hydroxide (NaOH), salicylic acid ($C_7H_6O_3$), sodium hypochlorite solution (NaClO), ethanol (CH_3CH_2OH), hydrazine hydrate ($N_2H_4 \cdot H_2O$) were purchased from Sinopharm Chemical Reagent Co., Ltd. (Shanghai, China). p-Dimethylaminobenzaldehyde (p-$C_9H_{11}NO$) and sodium nitroferricyanide dihydrate ($C_5FeN_6Na_2O \cdot 2H_2O$) were purchased from Tianjin Damao Chemical Reagent Factory.

2.2. Synthesis of WO_3

Using $NaWO_4 \cdot 2H_2O$ as the tungsten source and HCl as the morphology-controlling agent, WO_3 was synthesized in situ on fluorine doped tin oxide (FTO) glass using a simple hydrothermal method. First, 0.2474 g $NaWO_4 \cdot 2H_2O$ and 0.2344 g monohydrate oxalic acid were separately dispersed in 20 mL pure water, and both solutions was stirred for 30 min to ensure complete dissolution. Furthermore, 10 mL of 3 M HCl was dropped in the $NaWO_4$ solution and stirred for 15 min; when a light-yellow precipitate was obtained, the monohydrate oxalic acid solution was added, and the mixture was stirred for 30 min, following which the precipitate disappeared. An FTO glass sheet was placed with the conductive surface facing up at the bottom of a 100 mL reactor. The precursor solution was then added into the reactor and heated at 140 °C for 3 h. After cooling, a dropper was used to retrieve the solution in the reactor. A layer of yellow H_2WO_4 precipitate had formed on the FTO glass. WO_3 can then be obtained after annealing H_2WO_4 in a muffle furnace at 500 °C for 1 h.

2.3. Synthesis of $SrWO_4$

Tetrabutyl titanate and $NaWO_4$ were used as the sources of titanium and tungsten, respectively. They were dissolved in 20 mL ethylene glycol according to the proportion (W: Sr = 1:1 molar ratio), and a white precipitate was obtained after stirring for 8 h; the suspension solution was spin-coated on the FTO at 2000 rps, dried in an oven at 100 °C for 10 min, and then the FTO was coated again and cycled five times, until a thin film was observed on the FTO. Finally, $SrWO_4$ was obtained by annealing the film at 550 °C for 3 h.

2.4. Synthesis of Ti-WO_3/$SrWO_4$

First, H_2WO_4 was synthesized in situ on the FTO using the hydrothermal method. Tetrabutyl titanate as the titanium source and $Sr(NO_3)_2$ as the strontium source were dissolved in 20 mL of ethylene glycol at a molar ratio of 1:1 to obtain a precursor solution. The precursor solution was spin-coated on the abovementioned H_2WO_4 film, dried in an oven at 100 °C for 10 min, and then calcined at 400 °C in a muffle furnace for 10 min; the drip-coating–drying–calcining cycle was performed five times. The final calcination was performed at 550 °C for 3 h to synthesize Ti–WO_3/$SrWO_4$. The intermediate products $SrCO_3$ and H_2WO_4 in the high-temperature heating process generated $SrWO_4$ while H_2WO_4 simultaneously generated WO_3, which shared the tungsten source with $SrWO_4$ at high temperature (Scheme 1).

2.5. Photoelectrochemical test

A 500 W Xe lamp was used to simulate sunlight to examine the PEC NH_3 synthesis performance of different samples. A composite photocathode was used as the working electrode to be illuminated; a Pt plate was the counter electrode, and Ag/AgCl was the reference electrode in the three-electrode system. The mass of the working electrode catalyst was 0.56 mg. The PEC NH_3 synthesis performance of composite materials was measured. The NRR was conducted in an H-cell electrolytic cell under room temperature and ambient pressure. As shown in Fig. 9, a light window was set on one side of the electrolytic cell such that the cathode was completely irradiated. The anode chamber and cathode chamber were separated using a Nafion 117 proton exchange membrane, allowing only protons to pass through to avoid NH_3 generation by reduction at the cathode, thereby again losing electrons at the anode and causing oxidation. During the test, a nitrogen atmosphere was introduced throughout to ensure that the electrolyte reached a saturated state. As a comparison, single chamber electrolyzer was used for NRR.

2.6. Calculation of NH_3 yield and Faradaic efficiency

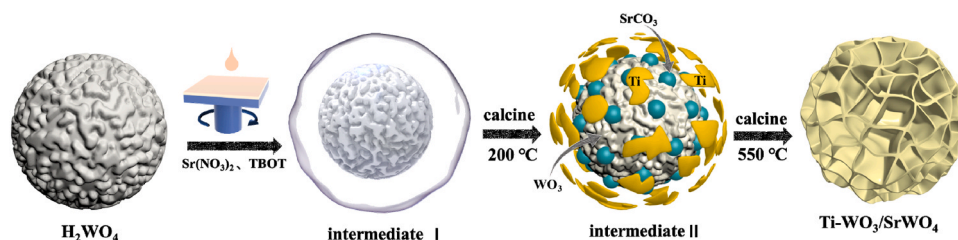#### 2.6.1. Quantification of NH_3

The concentration of synthetic NH_3 was determined using the indophenol blue method. Typically, 4 mL of the reacted electrolyte was obtained from the cathode cell and the absorber cell each. To the reacted electrolyte sample, 2 mL of 1 M NaOH solution (containing 5 wt% salicylic acid, 5 wt% sodium citrate) was separately added, followed by 1 mL of 0.05 M NaClO and 0.2 mL of 1 wt% $C_5FeN_6Na_2O$ to each. After mixing all the reagents, a yellow–green solution was obtained. The mixture was left to stand for 2 h under lightproof conditions, and the absorbance at $\lambda = 655$ nm was recorded using an ultraviolet (UV)–visible light (Vis) spectrophotometer. To determine the relationship between the amount of NH_3 and absorbance, calibration curves were plotted for NH_4Cl solutions of 0, 0.1, 0.3, 0.5, 0.7, and 0.9 μg/mL in 0.05 M H_2SO_4 and 0.1 M HCl. The calibrated fitted curve ($y = 0.5656x + 0.0465$, $R^2 = 0.999$) in 0.05 M H_2SO_4 shows the linear relationship between the absorbance spectrum and NH_3 concentration.

2.6.2. Quantification of N_2H_4

The concentration of hydrazine was quantified using the method of Watt and Chrisp. In this method, 5 mL of the reacted solution was obtained from the cathode cell; 5 mL of a chromogenic reagent was added, and the solution turned light blue. The solution was left for 2 h under lightproof conditions, and the UV–vis absorbance was measured at 455 nm. The chromogenic reagent was prepared by mixing p-(dimethylamino) benzaldehyde (5.99 g), HCl (concentrated, 30 mL), and ethanol (300 mL). To measure the amount of N_2H_4 produced, a calibration curve was plotted for concentrations of 0.1, 0.3, 0.5, 0.7, 0.9 μg/mL of N_2H_4 solution in 0.05 M H_2SO_4. The calibrated fitted curve ($y = 0.0697x + 0.0742$, $R^2 = 0.999$) shows the linear relationship between the absorbance spectrum and N_2H_4 concentration.

2.6.3. Faradaic efficiency

Assuming that three electrons are required to form an NH_3 molecule, the Faradaic efficiency in 0.05 M H_2SO_4 can be calculated as Eq. (2):

Scheme 1. Schematic illustration for preparing Ti-WO₃/SrWO₄.

$$FE = \frac{3 \times F \times C \times V}{17 \times Q} \qquad (2)$$

where F is the Faradaic constant (96,485 C mol^{-1}); C is the concentration of the generated NH₃; V is the volume of the electrolyte (30 mL); Q is the amount of charge in the PEC process.

2.7. Characterization

The crystal structures of samples were evaluated using X-ray diffraction (XRD, Bruker D8 Advance, German) analysis in the range of 10–90°. UV–Vis diffuse reflectance spectroscopy (DRS) was performed using Agilent Cary 100 (America) instrument over a range of 200–800 nm. The Raman spectra was tested via the Raman spectrometer (Horiba LabRAM HR Evolution, Japan). X-ray photoelectron spectroscopy (XPS) images of the photocatalysts were obtained using a Thermo Scientific K-Alpha instrument. Scanning electron microscopy (SEM) images were recorded on a Zeiss Gemini 300 microscope. Transmission electron microscopy (TEM) was performed using a JEOL-JEM-2100F microscope. Photoluminescence (PL) spectra were recorded on a F-2500 fluorescence spectrophotometer (Hitachi), excited at 540 nm. Electrochemical impedance spectroscopy (EIS) was performed and the photocurrent response of the catalyst investigated on the CHI760E electrochemical workstation in a standard three-electrode configuration.

2.8. Theoretical computation

The first-principles computations were performed based on density functional theory (DFT) with Vienna Ab-initio Simulation Package (VASP) codes 5.4 [36,37]. The Perdew–Burke–Ernzerhof (PBE) exchange–correlation functional of the generalized gradient approximation (GGA) [38], and a plane wave cut-off of 450 eV was used in the calculations. For a better description of the van der Waals correction, the DFT-D3 method was adopted with the PBE functional [39]. A slab with a WO₃ (010) surface and SrWO₄ (001) surface was then developed. The optimized WO₃ bulk with lattice constants a = 7.62 Å, b = 7.68 Å, and c = 7.71 Å and a = 90°, b = 90°, and g = 90°. The optimized SrWO₄ bulk with lattice constants a = 5.29 Å, b = 5.29 Å, c = 11.93 Å, and a = 90°, b = 90°, and g = 90°. A vacuum spacing over 20 Å was developed to avoid virtual interactions. The Brillouin zone was sampled with a 2 × 2 × 1 Monkhorst–Pack k-point mesh for electronic calculations. The convergence of energy and force were $< 10^{-5}$ eV and 0.02 eV/Å, respectively.

The reaction route was determined by calculating the change in free energy (ΔG) for each step in N₂ reduction as follows: $\Delta G = \Delta E + \Delta E_{ZPE} - T\Delta S$. ΔE is the change in total energy; ΔE_{ZPE} and ΔS are the energy differences in zero-point energy and entropy, respectively; T = 298.15 K. The zero-point energy and entropy were obtained by determining the vibrational frequencies, where all 3 N degrees of freedom are considered as harmonic vibrational motions while ignoring the contributions of the slab. Assuming pH = 0, the effect of pH on the NRR can be ignored. The preprocessing and postprocessing for the calculation were completed using VASPKIT software [40].

3. Results and discussion

3.1. Characterization of catalysts

Fig. 1a shows the XRD patterns of FTO, WO₃, SrWO₄, WO₃/SrWO₄, and Ti-WO₃/SrWO₄ photoelectrodes. For the FTO substrates, the characteristic peaks were located at 2θ = 26.3°, 33.2°, 37.6°, 42.7°, 51.3°, and 65.4° corresponding to the (110), (101), (200), (211), (310), and (301) crystal planes of SnO₂ (JCPDS: 46–1088) [41]. After WO₃ was grown on the FTO substrate, new 2θ diffraction peaks were observed at 23.25°, 23.74°, 24.47°, 26.7°, 34.28°, 41.75°, 47.34°, 50.03°, and 54.89° corresponding to the (002), (020), (200), (120), (202), (222), (004), (−2 to 23), and (0−42) crystal planes of monoclinic phase WO₃ (JCPDS:71-0305), respectively [42]. For WO₃/SrWO₄, the distinct peaks observed at 2θ = 18.11°, 27.79°, 29.99°, 33.19°, 37.99°, 45.28°, and 55.92° were identified as peaks of SrWO₄ (JCPDS:89–2568). The primary XRD peaks of Ti-WO₃/SrWO₄ are similar to those of WO₃/SrWO₄. However, because the doped Ti is amorphous, the diffraction peak of Ti ions cannot be detected in Ti-WO₃/SrWO₄. Our subsequent experiments proved the presence of Ti.

Fig. 1b shows the fluorescence spectra of SrWO₄, WO₃, WO₃/SrWO₄, and Ti-WO₃/SrWO₄. SrWO₄ and WO₃ had the highest fluorescence, and the fluorescence intensity considerably decreased after the complexation, indicating a reduction in the complexation of photoexcited electron-hole pairs. The lower fluorescence intensity after Ti doping was attributed to as the reduction in the number of excited electrons caused by Ti doping, which in turn reduced the chance of an electron jumping back to the ground state. Fig. 1c shows the UV–Vis spectra of SrWO₄, WO₃, WO₃/SrWO₄, and Ti–WO₃/SrWO₄. The SrWO₄ spectrum exhibits intense absorption across the UV wavelengths. After compounding with WO₃, the absorption edge of WO₃/SrWO₄ exhibited a slight red shift. Compared with WO₃/SrWO₄, the absorption edge of Ti–WO₃/SrWO₄ was ~500 nm, indicating that Ti–WO₃/SrWO₄ promotes improved utilization of visible light, primarily because of doping with Ti ions. Moreover, the corresponding gap energies of SrWO₄, WO₃, WO₃/SrWO₄, and Ti–WO₃/SrWO₄ were reported to be 2.9, 2.45, 2.3, and 2.4 eV, respectively, as per the Huckel relationship: $\alpha h\nu = A (h\nu\text{-Eg})^{n/2}$ where hν is the abscissa and $(\alpha h\nu)^2$ is the ordinate (Fig. 1d). As shown in Raman spectra from 100 to 1100 cm^{-1} (Fig. S3), SrWO₄ has three vibrational modes: Bg (ν3, 833 cm^{-1}), Eg (ν3, 799 cm^{-1}), Bg (ν4, 372 cm^{-1}). The vibration modes for peaks at 336 and 373 cm^{-1} are attributed to the antisymmetric and symmetric bending of WO₄$^{2-}$ [43]. The vibration modes near 798 and 836 cm^{-1} are attributed to the asymmetric stretching of WO₄. Moreover, these modes appear in the Raman spectra of WO₃/SrWO₄ and Ti–WO₃/SrWO₄. Four Raman bands of monoclinic WO₃ can be clearly observed. The Raman bands at 704 and 802 cm^{-1} originate from the O–W–O stretching vibration mode, while those at 265 and 321 cm^{-1} are attributed to the O–W–O bending vibration mode of WO₃ [44]. After doping with Ti, the peak height of the composite slightly decreased. Because of the overlap of metal–oxygen bonds, the Raman peaks of the W–O–W vibrations in the WO₃/SrWO₄ composite photocatalyst were diminished.

As shown in Fig. 2a, the thickness of the Ti–WO₃/SrWO₄ film is ~50 nm. Fig. 2b shows the surface morphology of the Ti–WO₃/SrWO₄.
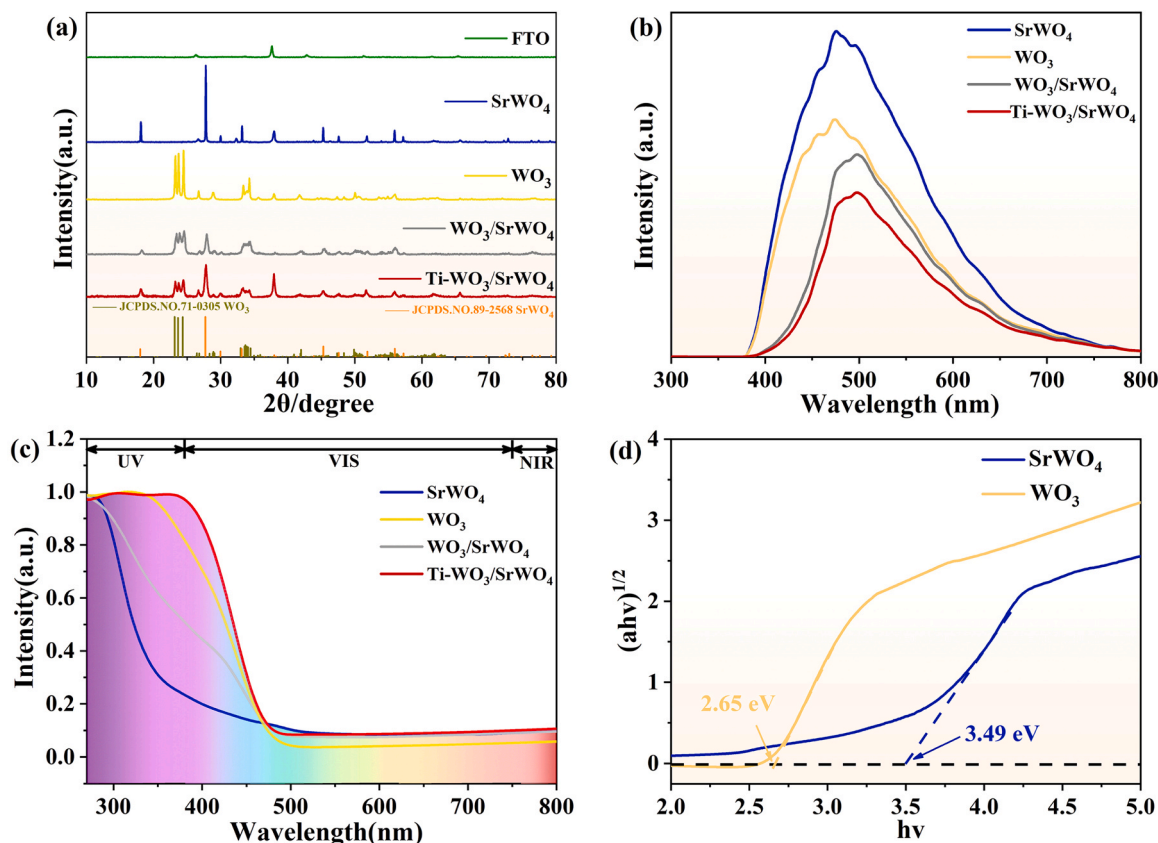
Fig. 1. (a) XRD patterns, (b) PL spectra, (c) UV–vis DRS spectra, and (d) plots of $(\alpha h\upsilon)^{1/2}$ versus $h\upsilon$ for of WO_3, $SrWO_4$, $WO_3/SrWO_4$ and $Ti\text{-}WO_3/SrWO_4$.
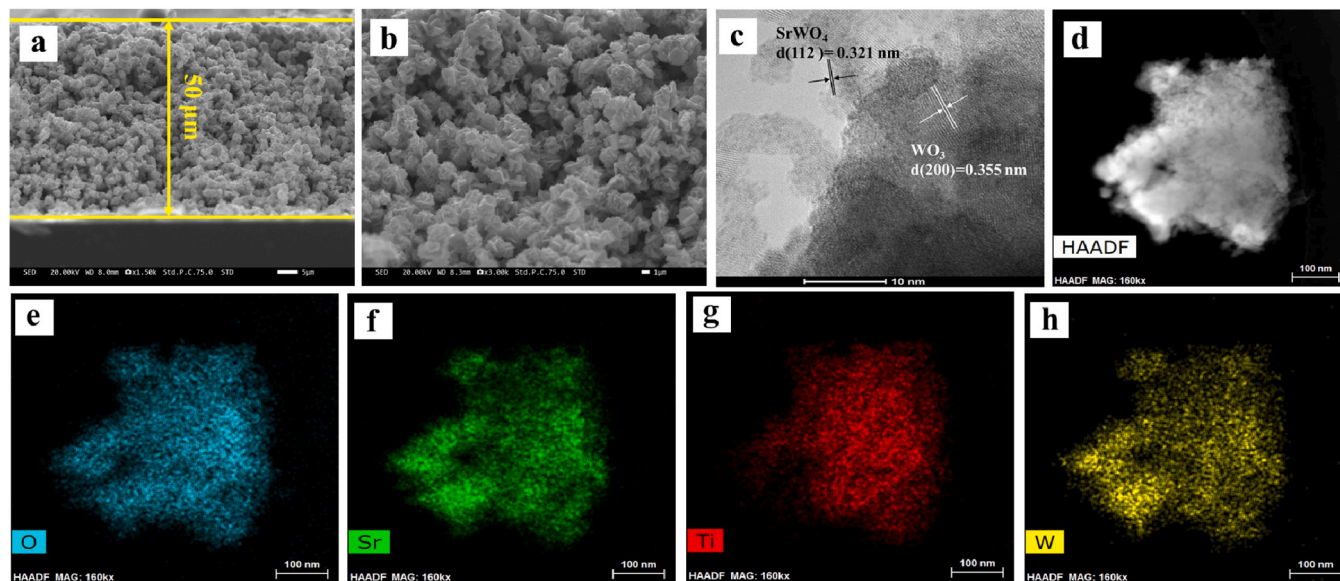

Fig. 2. SEM images of the $Ti\text{-}WO_3/SrWO_4$ film: (a) cross-sectional morphology and (b) Surface morphology of the film. (c, d) TEM image and (e-h) elemental mapping images of $Ti\text{-}WO_3/SrWO_4$.

The $Ti–WO_3/SrWO_4$ film was composed of flower-like particles with a diameter of ~1 μm. $Ti\text{-}WO_3/SrWO_4$ coated with only one layer of precursor grows vertically perpendicular to the FTO (Fig. S1). Fig. 2c shows the HRTEM results for a clean interface of the $Ti–WO_3/SrWO_4$ heterojunction. Furthermore, the HRTEM image shows that the lattice space of 0.386 and 0.355 nm are attributed to the (200) and (020) crystal planes of WO_3, respectively. The lattice space with spacings of 0.321 nm

corresponds to the (112) facets of tetragonal $SrWO_4$, suggesting that the $Ti–WO_3/SrWO_4$ heterojunction has high crystallinity. The results of EDS mapping of $Ti–WO_3/SrWO_4$, as shown in Fig. 2d–h, validate the presence of W, Ti, O, and Sr. This result indicates that Ti ions were effectively incorporated into the $WO_3/SrWO_4$ structure.

The XRD patterns of the used $Ti–WO_3/SrWO_4$ heterojunctions were essentially similar to those of the fresh $Ti–WO_3/SrWO_4$ heterojunctions,

and no noticeable deviation was observed, indicating the high stability of Ti–WO₃/SrWO₄ samples (Fig. 3a). However, the color of the fresh and used Ti–WO₃/SrWO₄ heterojunctions were clearly different (inset Fig. 3a). PEC NRR was predicted to influence the surface chemical state of the Ti–WO₃/SrWO₄ photoanode, thus resulting in a change in the color of the used sample. Therefore, the chemical interfaces and binding states of the fresh and used Ti–WO₃/SrWO₄ heterojunctions were examined using XPS. As shown in Fig. 3b, the survey spectrum shows that the fresh and used Ti–WO₃/SrWO₄ heterojunctions were composed of W, Sr, Ti and O. The high-resolution spectrum of Sr 3d is shown in Fig. 3c. The peaks at 133.07 and 134.77 eV are attributed to the Sr 3d of Sr^{2+}. Moreover, the W $4f_{5/2}$ and W $4f_{7/2}$ states can be observed at 35.4 and 37.5 eV, suggesting that W exists as W^{6+}(Fig. 3d). From Fig. 3e, we see that the peaks of Ti 2p can be fitted into four peaks; the peaks at 458.94 and 464.53 eV are attributed to the Ti 2p of Ti^{3+}, and those at 459.36 and 465.23 eV are attributed to the Ti 2p of Ti^{4+}. These peaks indicate that both Ti^{3+} and Ti^{4+} were successfully introduced. For the O1s core-level spectra, two peaks can be clearly identified (Fig. 3f)—the peak at 530.37 eV is attributed to metal–oxygen bonds (W-O bond in SrWO₄ and WO₃), and that at 531.97 eV is associated with the hydroxy species of surface-adsorbed water molecules. The fresh and used Ti–WO₃/SrWO₄ heterojunctions contribute 10.7 % and 37.5 % of 531.97 eV components of the whole O1s. The abovementioned results indirectly prove that the as-prepared Ti–WO₃/SrWO₄ heterojunctions have excellent hydrophilic properties, which are conducive to providing abundant hydrogen protons for NH₃ production.

3.2. PEC properties of Ti-WO₃/SrWO₄

The transfer and separation efficiencies of the charge carriers on the interface of Ti–WO₃/SrWO₄ heterojunctions were examined by performing linear sweep voltammetry (LSV) and EIS and obtaining the photocurrent response and the applied bias photon to current efficiencies (ABPE). The LSV curves of different electrode materials in 0.05 M H₂SO₄ electrolyte under AM 1.5 G (100 mW/cm²) light are shown in Fig. 4a. The photocurrent densities of SrWO₄ and WO₃ are − 0.15 and − 0.41 mA/cm² at − 0.6 V vs. RHE, respectively. After

combining SrWO₄ with WO₃, the photocurrent density reached − 1.05 mA/cm² at − 0.6 V vs. RHE. When Ti was doped into WO₃/SrWO₄, the photocurrent density clearly increased up to − 2.05 mA/cm², which is 1.95 times that of WO₃/SrWO₄. This result indicates that Ti doping promotes the charge-separation and light absorption properties of WO₃/SrWO₄ photoanodes.

Fig. 4b shows the EIS curves of SrWO₄, WO₃, WO₃/SrWO₄, and Ti–WO₃/SrWO₄. In the figure, a smaller semicircle radius indicates better charge transfer capability (i.e., faster surface reaction kinetics). The extremely small semicircle radius of the Ti–WO₃/SrWO₄ electrode indicates a much higher interfacial charge-transfer rate was achieved on the Ti–WO₃/SrWO₄ photoanode compared to that on the other electrodes.

Fig. S4a shows the LSV diagram corresponding to the reaction in darkness. The electrochemical performance of Ti–WO₃/SrWO₄ in darkness is still prominent. The initial potential of the electrode in darkness shifts backward compared with that observed under illumination. The considerably enhanced current at the same voltage indicates that Ti doping provides an abundance of active sites for the reaction. However, the current density of the electrode is extremely low—in the range of 0.4–0.5 V vs. RHE voltage for the photocatalytic NH₃ synthesis reaction. Furthermore, the EIS spectrum (Fig. S4b) obtained under dark conditions yielded the same results as those obtained via the LSV analysis. In darkness, the reaction kinetics at the electrode–electrolyte interface increased, the carrier transport was blocked, and the electron–hole separation efficiency decreased.

Fig. S5a shows the photocurrent response spectra of WO₃, SrWO₄, WO₃/SrWO₄, and Ti–WO₃/SrWO₄. The photocurrent was < 1 μA for both pure WO₃ and SrWO₄. The photocurrent of WO₃/SrWO₄(3.8 μA) was higher than that of SrWO₄, indicating that combination with WO₃ resulted in a low photogenerated carrier recombination efficiency. The photocurrent produced by Ti–WO₃/SrWO₄(4.8 μA) was the highest among all samples, demonstrating that Ti–WO₃/SrWO₄ has the highest charge separation efficiency. Furthermore, the photocurrent is extremely stable in continuous on/off cycles.

The ABPE shows the photocurrent conversion efficiency under an applied bias. The calculated ABPE of all the samples are shown in
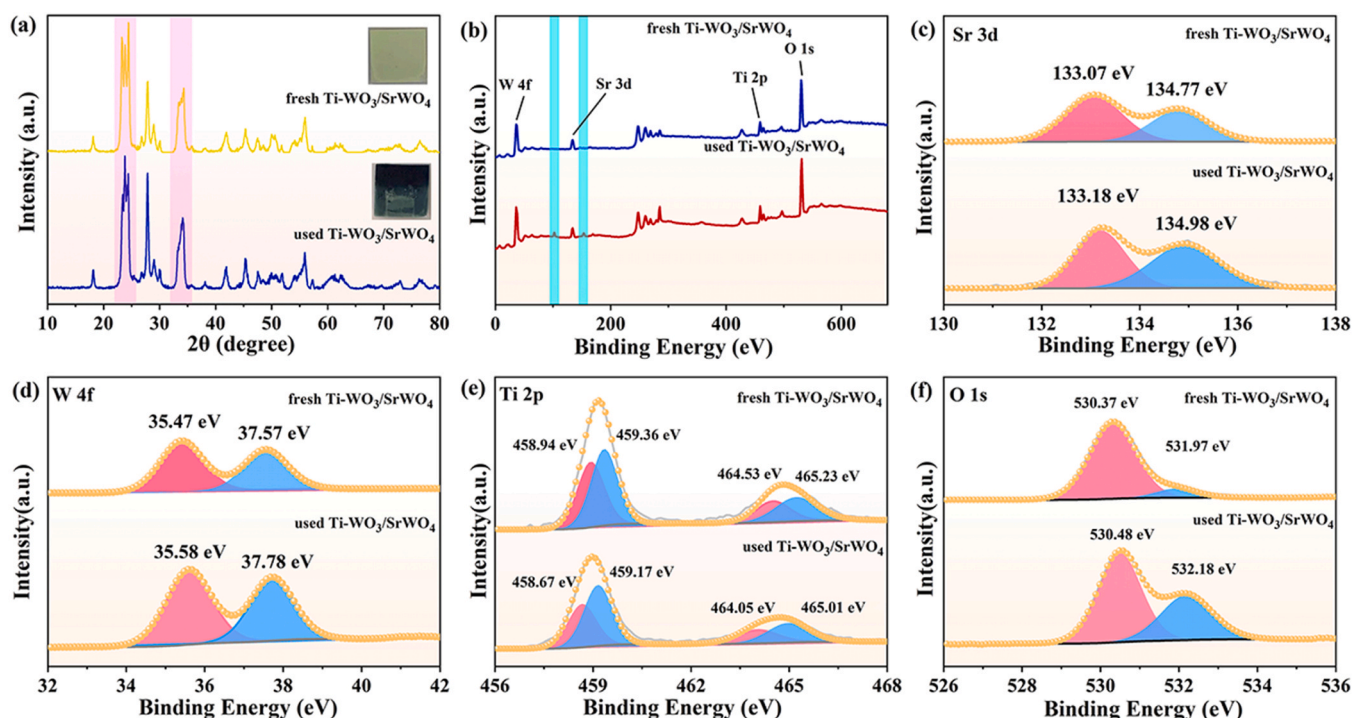

Fig. 3. (a) XRD patterns, (b) XPS profiles, (c-f) Sr/W/Ti/O bonding states in the fresh and used Ti-WO₃/SrWO₄.
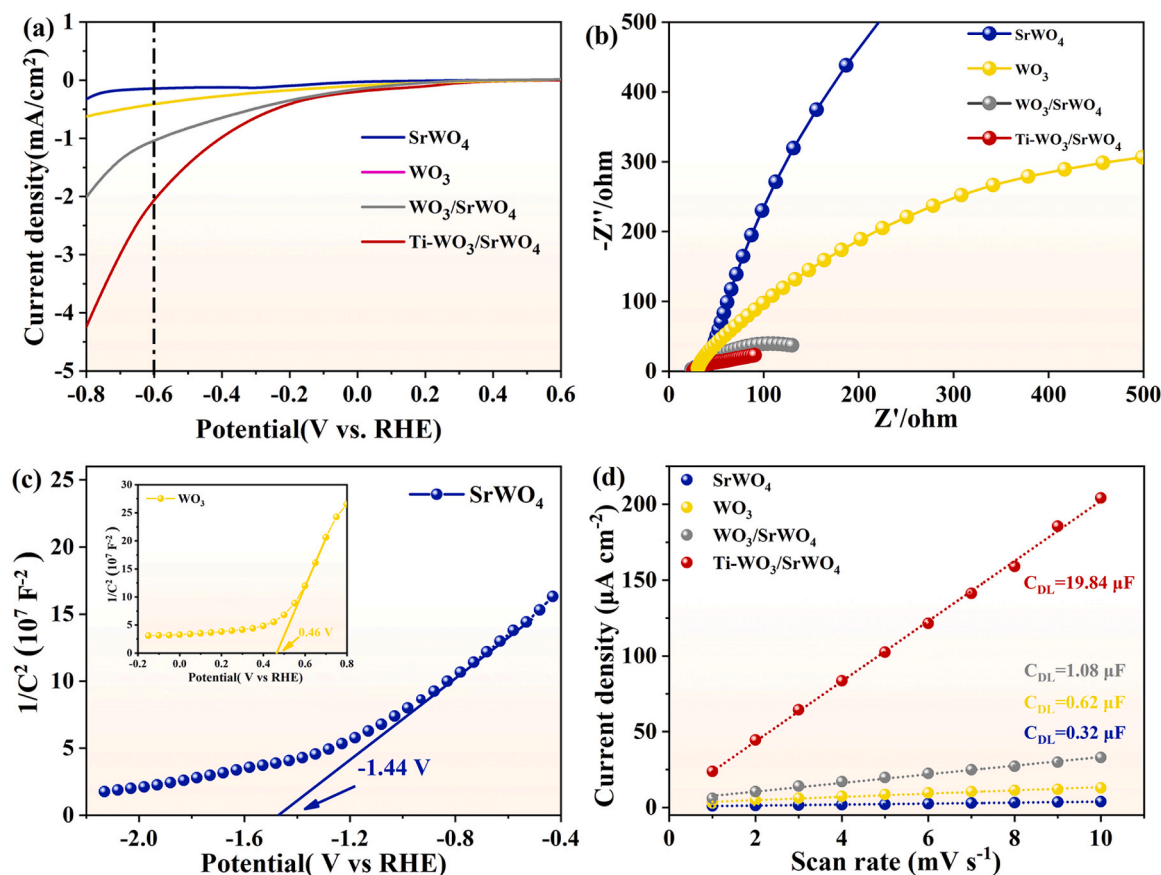
Fig. 4. (a) LSV curve, (b) EIS diagram of $SrWO_4$, WO_3, $WO_3/SrWO_4$ and $Ti-WO_3/SrWO_4$, (c) Mott-Schottky curves of pure $SrWO_4$ and $Ti-WO_3/SrWO_4$, (d) Charging current density differences of $SrWO_4$, WO_3, $WO_3/SrWO_4$ and $Ti-WO_3/SrWO_4$ plotted against scan rates.

Fig. S5b. The ABPE of $SrWO_4$ and WO_3 at 0.6 V vs. RHE were only 0.04 % and 0.12 %, respectively. The ABPE of the $WO_3/SrWO_4$ composite electrode was 0.32 %, which is eight times and 2.6 times that of pure $SrWO_4$ and WO_3 electrodes, respectively. The ABPE of $Ti–WO_3/SrWO_4$ reached 0.62 %, which is considerably higher than that of the $WO_3/SrWO_4$ electrodes. These results clearly demonstrate that the formation of $Ti–WO_3/SrWO_4$ nanojunctions effectively improves the PEC performance of $SrWO_4$ photoanodes.

The results of the Mott–Schottky test show that $SrWO_4$ and WO_3 are N-type semiconductors (Fig. 4c) with a flat-band potential of − 1.44 and 0.46 eV, respectively. Because the flat band potential of N-type semiconductors is close to the conduction band (CB) and is ~0.3 eV lower than the CB, the CB of $SrWO_4$ and WO_3 is − 1.14 and 0.76 eV, respectively. As per the equation $Eg = E_{CB} − E_{VB}$, the CB and valence band (VB) of $SrWO_4$ are calculated to be − 1.14 and − 4.63 eV, respectively, and those of WO_3 are calculated to be 0.76 and − 1.89 eV, respectively. $SrWO_4$ and WO_3 form an n–n type heterojunction, which limits the compounding of photogenerated carriers and facilitates the transport of photogenerated electrons.

Furthermore, to determine the overall enhancement of photocurrent density as a function of wavelength, the incident photon-to-current conversion efficiency (IPCE) values of $SrWO_4$, WO_3, $WO_3/SrWO_4$, and $Ti–WO_3/SrWO_4$ electrodes were measured at a bias of − 0.6 V vs. RHE. As shown in Fig. S6a, the maximum IPCE value of the $Ti–WO_3/SrWO_4$ electrode reached 7.9 % at 359 nm, which is considerably higher than that of the $SrWO_4$ photoanode (1.45 % at 359 nm). In the 520–600 nm range, $Ti–WO_3/SrWO_4$ exhibits varying degrees of improvement in the photovoltaic conversion efficiency compared to $SrWO_4$. The maximum APCE of $Ti–WO_3/SrWO_4$ reached 7.27 % at 359 nm (Fig. S6b), which was considerably higher than that of the $SrWO_4$ photoanode (1.36 % at

359 nm). These results confirm that Ti doping improves the photoelectric conversion efficiency.

To compare the electrochemical active surface area (ECSA), we examined the CV curve (Fig. S9) of electrodes in the range of 0.396–0.496 V vs. RHE The ΔJ value gradually increased as the sweep speed increased from 10 to 100 mV/s. The electrochemical double-layer capacitance (C_{DL}) values of $SrWO_4$, WO_3, $WO_3/SrWO_4$, and $Ti–WO_3/SrWO_4$ at 0.446 V vs. RHE were 0.32, 0.62, 1.08, 19.84 μF, respectively. (Fig. 4c).

The ECSA is estimated by the Eq. (3):

$$ECSA = \frac{C_{DL}}{C_S} \tag{3}$$

where Cs is the specific capacitance of the electrode, i.e., the capacitance of the smooth plane of the same material measured under the same electrolyte conditions. It is not practical to synthesize a catalyst with a smooth surface by spin-coating; however, as per the existing C_{DL}, we can draw a general conclusion. The Cs of the electrode in the H_2SO_4 solution is 0.033 mF cm^{-2}, according to the measurements reported in literature [45]. Therefore, the ECSA values of $SrWO_4$, WO_3, $WO_3/SrWO_4$, and $Ti–WO_3/SrWO_4$ are 0.01, 0.02, 0.03, 0.60 cm^{-2}, respectively.

3.3. PEC NRR activity assessment

Fig. 9 shows the H-cell electrolytic cell used for the synthetic NH_3 test. In the figure, the cathode cell (right) is the reaction cell, and $Ti–WO_3/SrWO_4$ is used as the cathode reaction electrode to undergo the NRR and the H_2 reduction reaction. NRR occurs in the anode cell (left). Before the reaction, N_2 gas was allowed to flow for 30 min to saturate the electrolyte solution. The effect of bias voltage on NH_3 synthesis was

examined (Fig. 5a), and Ti–WO_3/$SrWO_4$ had the greatest influence on NH_3 synthesis at a voltage of -0.5 V vs. RHE, reaching a maximum of 11.17 µg h^{-1} cm^{-2}. Under a larger bias voltage (-0.6 V vs. RHE), a hydrogen evolution competition reaction may occur, resulting in a lower NH_3 synthesis efficiency of 3.76 µg h^{-1} cm^{-2}. The NH_3 synthesis efficiency of both $SrWO_4$ and WO_3 is extremely low and does reach 3 µg h^{-1} cm^{-2} (Fig. 5b). After the two were combined, the NH_3 synthesis efficiency was considerably improved. The efficiency exceeded 5.99 µg h^{-1} cm^{-2}, which is consistent with the results obtained after Ti doping. Selective vulcanization greatly affects NRR because of the improved electron transport efficiency realized by Ti doping. By donating electrons to nitrogen, Ti^{3+} gets chemically adsorbed and forms acts as sites for nitrogen activation. Under the excitation of simulated sunlight, the photogenerated electrons are captured by the electrode element W; such electron recapture is beneficial to the regeneration of Ti^{3+} activation sites. Furthermore, we determined the amount of intermediate

hydrazine in the solution (Fig. 5c). The results demonstrated that the hydrazine yield does not reach 0.1 µg h^{-1} cm^{-2}, indicating that the catalysts have high selectivity and a distal pathway of the NRR. However, under -0.5 V vs. RHE, the yield of the intermediate hydrazine in the nitrogen reduction of Ti–WO_3/$SrWO_4$ was higher, indicating that the NRR on Ti–WO_3/$SrWO_4$ is an associative hydrogenation pathway. N_2 is activated in the second step to generate N_2H_4 in the associative hydrogenation pathway. Because of the high activation towards the NRR and high overpotential to HER, the Faradaic efficiency of Ti–WO_3/$SrWO_4$ was 13.42 % at -0.5 V vs RHE. Table S1 shows a comparison of the synthetic ammonia yield of Ti–WO_3/$SrWO_4$ with other catalysts reported, concluding that the yield of Ti–WO_3/$SrWO_4$ is superior. In addition, we tested the effect of Ti–WO_3/$SrWO_4$ on ammonia synthesis in a single chamber cell electrolyzer. At -0.5 V vs. RHE, the ammonia production of $SrWO_4$, WO_3, WO_3/$SrWO_4$ and Ti–WO_3/$SrWO_4$ is much lower than that in the H-cell. The Faraday efficiency is also reduced
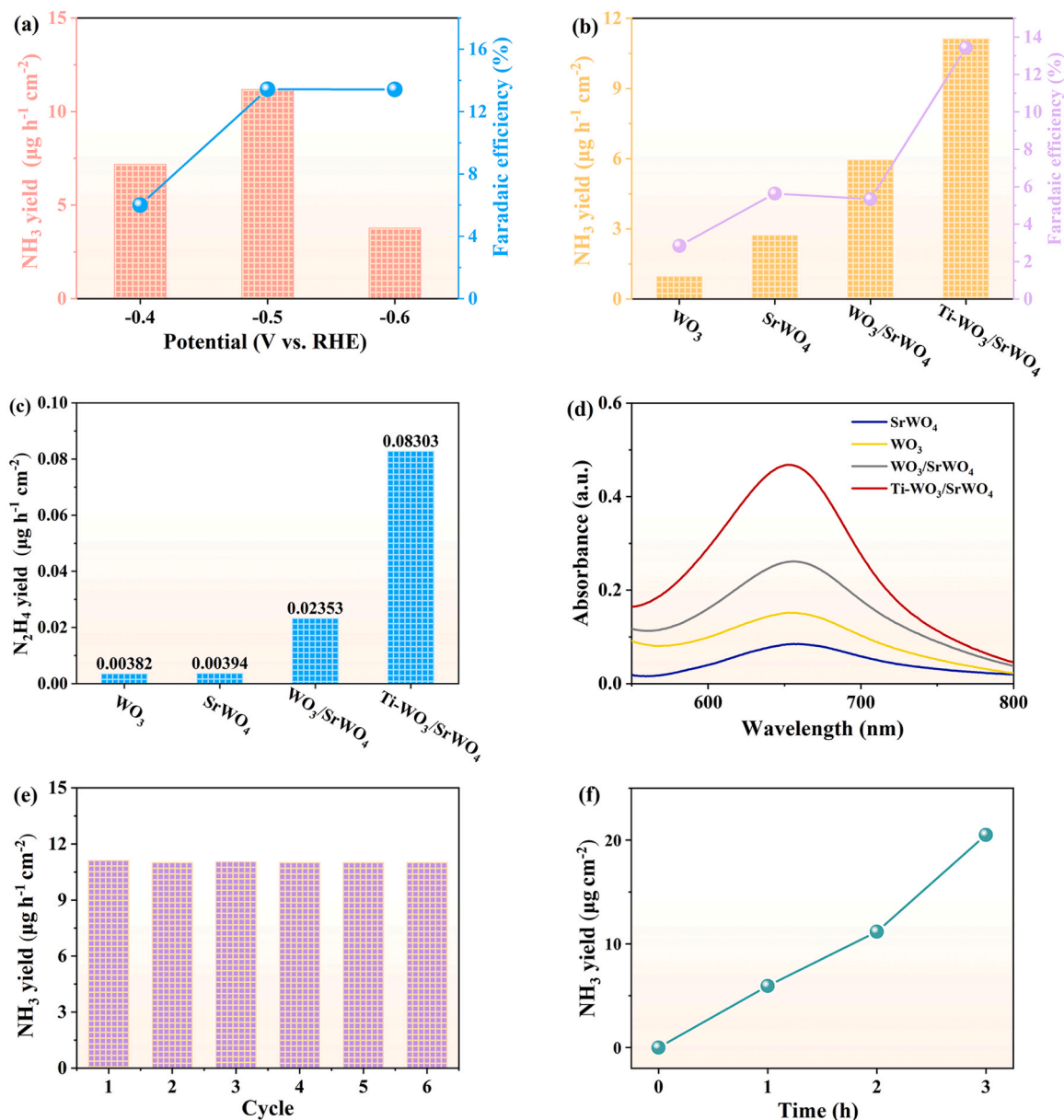

Fig. 5. (a) Ammonia formation rates (the average value on 2 h reaction), (b) Hydrazine formation rate, (c) corresponding Faradaic efficiencies and (d) UV-Vis absorption spectra of the electrolytes colored with indophenol blue indicator at -0.5 V vs. RHE after NRR. (e) The stability of the photocatalytic performance of Ti-WO_3/$SrWO_4$ by 6 repeated photoelectrocatalytic cycles. (f) The linear relation between reaction time and the ammonia yield for Ti-WO_3/$SrWO_4$ at -0.5 V vs. RHE.

accordingly (Fig. S10).

The stability of Ti–WO$_3$/SrWO$_4$ was confirmed using cyclic experiments (Fig. 5e) and cumulative nitrogen fixation experiments (Fig. 5f). Through three cycles of experiments, the output of the photoelectric NH$_3$ synthesis of Ti–WO$_3$/SrWO$_4$ reached > 2.6 mmol h^{-1} g$_{cat}^{-1}$. Subsequently, a Ti–WO$_3$/SrWO$_4$ nitrogen fixation test was performed at − 0.5 V vs RHE for 3 h. The NH$_3$ concentration in the electrolyte was measured every hour. Fig. 5f shows the relationship between reaction time and NH$_3$ yield; the figure shows a good linear relationship between the two.

The PEC NRR test was performed to determine the nitrogen reduction ability of the catalyst Ti–WO$_3$/SrWO$_4$ by LSV. LSV measurements

(Fig. 6a) were performed in an Ar and N$_2$ saturated environment to differentiate between the HER and NRR. As shown in the figure, the photocurrent density is significantly different in the N$_2$-saturated solution and the Ar-saturated solution, and the difference becomes more prominent with the increase in the bias voltage. Ti–WO$_3$/SrWO$_4$ has a higher photocurrent response under nitrogen, indicating that this electrode has excellent NRR performance. Within the range of the bias voltage applied in the test, the competitive response of HER is less than that of NRR. Fig. 6b and c show that there is no NH$_3$ in the electrolyte saturated with Ar. Fig. 6d shows the photoelectrochemical stability of the electrode. To ensure that the experimental data are true and have practical application value, we performed a 12 h stability test in 20
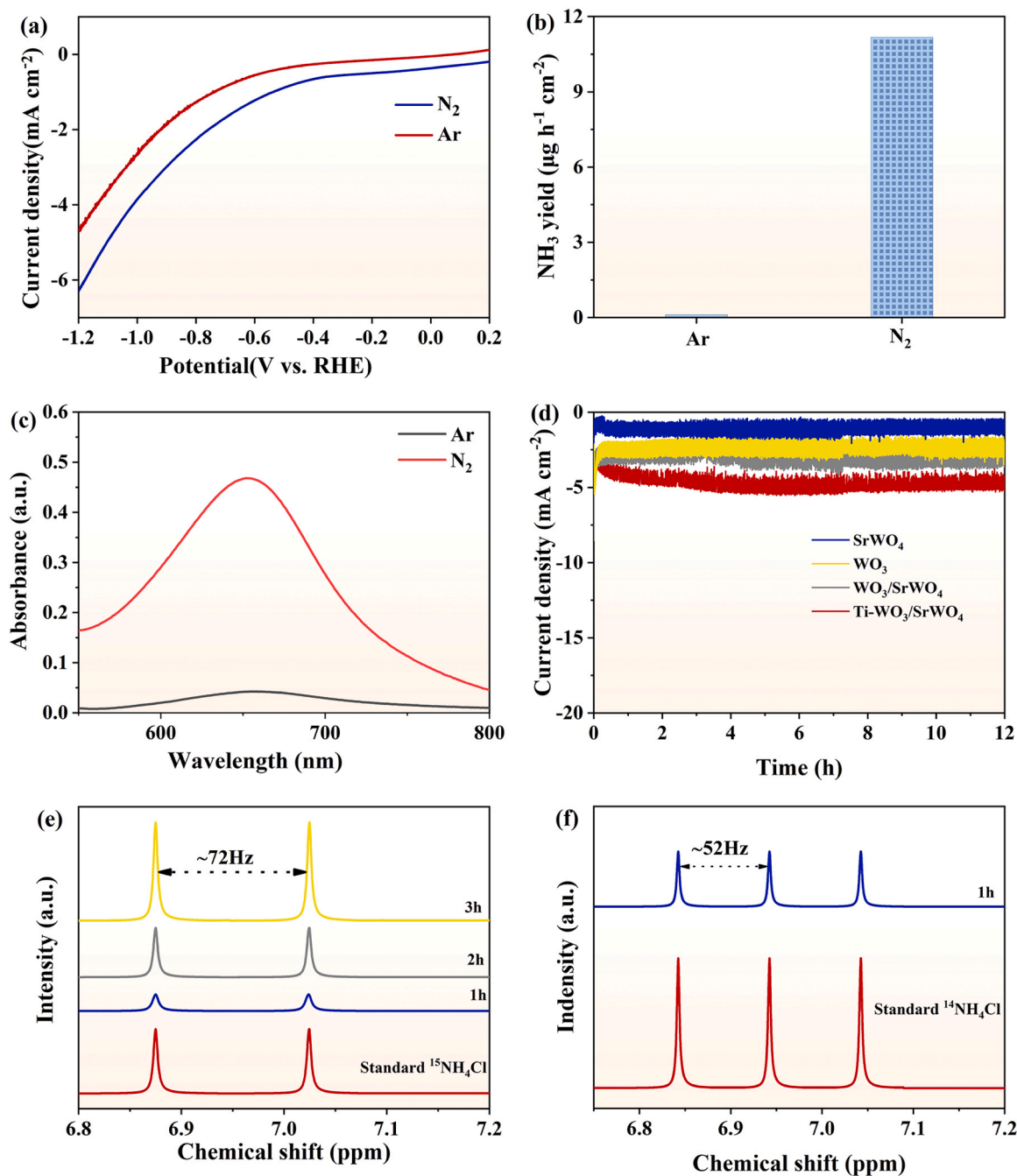

Fig. 6. (a) LSV curves of Ti-WO$_3$/SrWO$_4$ in N$_2$ and Ar saturated electrolyte of Ti-WO$_3$/SrWO$_4$. (b) Ammonia formation rates of Ti-WO$_3$/SrWO$_4$ in Ar ang N$_2$ at − 0.5 V vs. RHE for 2 h. (c) UV-Vis absorption spectra of the electrolytes colored with indophenol blue indicator in Ar ang N$_2$ after NRR. (d) Stability test of WO$_3$, SrWO$_4$, WO$_3$/SrWO$_4$ and Ti-WO$_3$/SrWO$_4$, Ti-WO$_3$/SrWO$_4$ at the potential of − 0.5 V vs. RHE. NMR spectra of 1 H for electrolytes after NRR test using 15 N$_2$ (e) and 14 N$_2$ (f) as feeding gas.

SCCM nitrogen flow. The stability of the electrode reached equilibrium after 0.5 h, and the performance almost did not decrease after 12 h, indicating that the electrode material has a certain practical application value.

To prove that the generated NH_4^+ is derived from the introduced gas N_2 and that the experiment is not disturbed by external air, we labelled $^{15}N_2$ in the experiment with isotopes and sampled at 1 h, 2 h, and 3 h within 3 h of testing. For comparison, the experimental results of N_2 as a gas source were also tested under identical conditions (Fig. 6e and f). To ensure the experimental accuracy, the nuclear magnetic hydrogen spectra of $^{14}NH_4Cl$ and $^{15}NH_4Cl$ were used as reference standards. As shown in Fig. 6e, all the measured peaks correspond to $^{15}NH_4^+$, and there is no impurity peak of $^{14}NH_4^+$. The peak area of $^{15}NH_4^+$ increases proportionally with time, and this result is consistent with Fig. 5f. Meanwhile, Fig. 6f confirms the formation of $^{14}NH_4^+$ when N_2 is used as a nitrogen source in the experiment.

3.4. Mechanism

We simulated the adsorption of N on Ti–WO_3/$SrWO_4$ and WO_3/$SrWO_4$ using the first-principles calculations to elucidate the role of Ti doping in N_2 adsorption. The charge density difference analysis shows that a considerable number of electrons are clustered on the Ti in the Ti–WO_3/$SrWO_4$ in the adsorbed N≡N bond (Fig. 7a). In comparison, there are fewer electrons in the N≡N bond to the W atom on WO_3/$SrWO_4$. The presence of a larger electron cloud between Ti and N_2 is a step that coincides with the N_2 adsorption energy, indicating that N_2 is more strongly adsorbed on Ti.

To gain insight into possible NRR mechanisms on Ti–WO_3/$SrWO_4$, the differences in the amount of NRR processes with and without Ti doping were further investigated by DFT calculations. The NRR results are shown in Fig. 5, where Fig. 5b shows the presence of N_2H_4 during the

Fig. 7. (a) Charge density difference of Ti-WO_3/$SrWO_4$, N_2/Ti-WO_3/$SrWO_4$ and N_2/WO_3/$SrWO_4$. The isosurface illustrates the configuration of electron accumulation (yellow) and depletion (blue) with the level of 0.0006 e$Å^{-3}$. (b) Calculated free energy diagram of NRR on Ti-WO_3/$SrWO_4$ and WO_3/$SrWO_4$ surfaces.

test. Hence, we calculated the change in free energy for the alternate hydrogenation mechanism. The chemisorption of N_2 on the Ti–WO_3/$SrWO_4$ surface is regarded a key to NRR kinetics. The free energy of N_2 on both materials is explained in Fig. 7b. The adsorption energy of the doped Ti–WO_3/$SrWO_4$ is − 0.39 eV, which is significantly higher than that of WO_3/$SrWO_4$ (ΔG = 0.28 eV). N_2 tends to spontaneously adsorb on the Ti in Ti–WO_3/$SrWO_4$. The first hydrogenation step (*N_2→ *NNH) is considered as a potential-determining step. This step shows a slight uphill path (ΔG = 3.46 eV), with the rest of the hydrogenation process is a spontaneous downhill release of energy. Notably, the steps from *NH_3 to NH_3(g) all exhibit an uphill pathway owing to the high solubility of the generated NH_3 in H_2SO_4, and therefore, these steps are not parts of the NRR step. Overall, the DFT analysis shows that Ti–WO_3/$SrWO_4$ can be an efficient NRR catalyst and that the NRR performance can be effectively enhanced by doping with Ti.

The density of states and the partial density of states for WO_3/$SrWO_4$ and Ti–WO_3/$SrWO_4$ are shown in Fig. 8. The zero-point energy marked with a short horizontal dashed line is set to the Fermi level in Fig. 7. Although both $SrWO_4$ and WO_3 are semiconductors, the two complexes have no remarkable band gap after compounding. This indicates that the atomic orbitals of $SrWO_4$ and WO_3 overlap, and the full band and forbidden band overlap to form the CB, thereby enhancing the conductivity of WO_3/$SrWO_4$ and Ti–WO_3/$SrWO_4$. Fig. 7c and d show that the bottom energy state of the CB is occupied by W atoms, and the doping of Ti shifts the d orbitals of W to the right (Fig. 7f), suggesting that Ti doping broadens the optical absorption range and induces the generation of electron–hole pairs more effectively under sunlight irradiation.

$SrWO_4$ has abundant emission spectra and spectral coordination, and hence, the electrons in the conduction band are easily excited to participate in the NRR during photocatalytic NH_3 synthesis. WO_3 has a wide light absorption range and high utilization of visible light, which are conducive for generating electron–hole pairs. Meanwhile, the heterojunction formed by $SrWO_4$ and WO_3 inhibits the recombination of photogenerated electrons and holes so that the photoexcited electrons can participate in the NRR as much as possible. In detail, electrons in the valence band (VB) of $SrWO_4$ are excited to the CB to produce electron–hole pairs. The electrons tend to compound with holes, and the compounding of WO_3 makes the electrons in the valence band of $SrWO_4$ jump to the valence band of WO_3 in this process. Meanwhile, the negative external bias consumes the photogenerated holes in $SrWO_4$, which can effectively promote the separation of electrons and holes and inhibit the recombination of photogenerated carriers. The photoelectric synergy process promotes PEC NRR more effectively. Ti is the main active center for the adsorption of N_2 and electrons, and the cycling of Ti^{3+} and Ti^{4+} facilitates the continuation of the reaction.

The NH_3 synthesis mechanism is divided into two types: dissociation and association mechanisms. Owing to the presence of hydrazine in our synthetic NH_3, the mechanism is judged to be a distal association mechanism. In the first step of the reaction, N_2 associates with the surface of the catalyst, as shown in Fig. 9. In the second step, the hydrogenation reaction first occurs on the N atom that is far away from the semiconductor. In the third step, the second hydrogenation reaction occurs on the N atom close to the semiconductor, so hydrogenation takes place in turn until two NH_3 molecules are generated simultaneously. A portion of the electrons on the surface of the catalyst participate in NH_3 synthesis, and the other part of the electrons change the valence state of the doped Ti to realize the nitrogen reduction cycle (Fig. 9). The reaction mechanism is divided into three steps. (1) Ti^{3+} adsorbs and activates nitrogen to break the first bond of the N≡N triple bond, and Ti^{3+} is oxidized to Ti^{4+}, which combines with the N≡N intermediate state to form an intermediate unstable state 1. (2) The electrons from the photoexcited semiconductor continue to reduce state 1, and the second N≡N bond is broken, and H^+ in the electrolyte solution H_2SO_4 participates in the hydrogenation reaction to generate an intermediate state 2. (3) N≡N is completely broken, and the hydrogenation and reduction
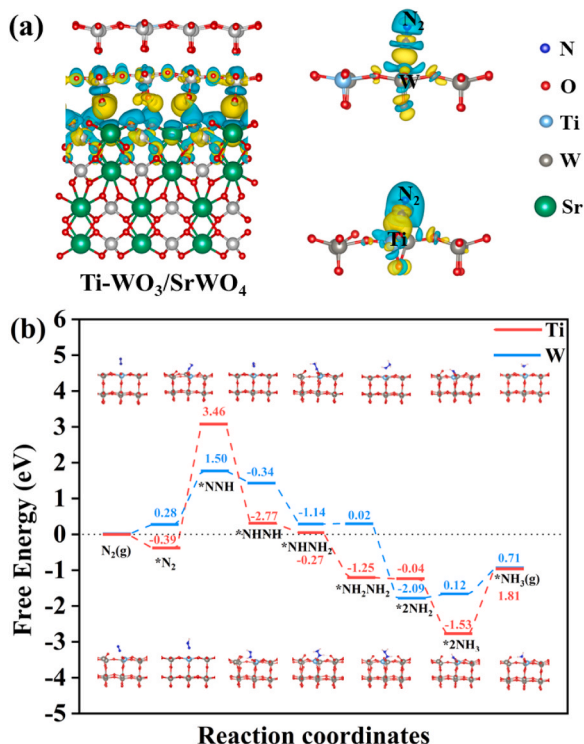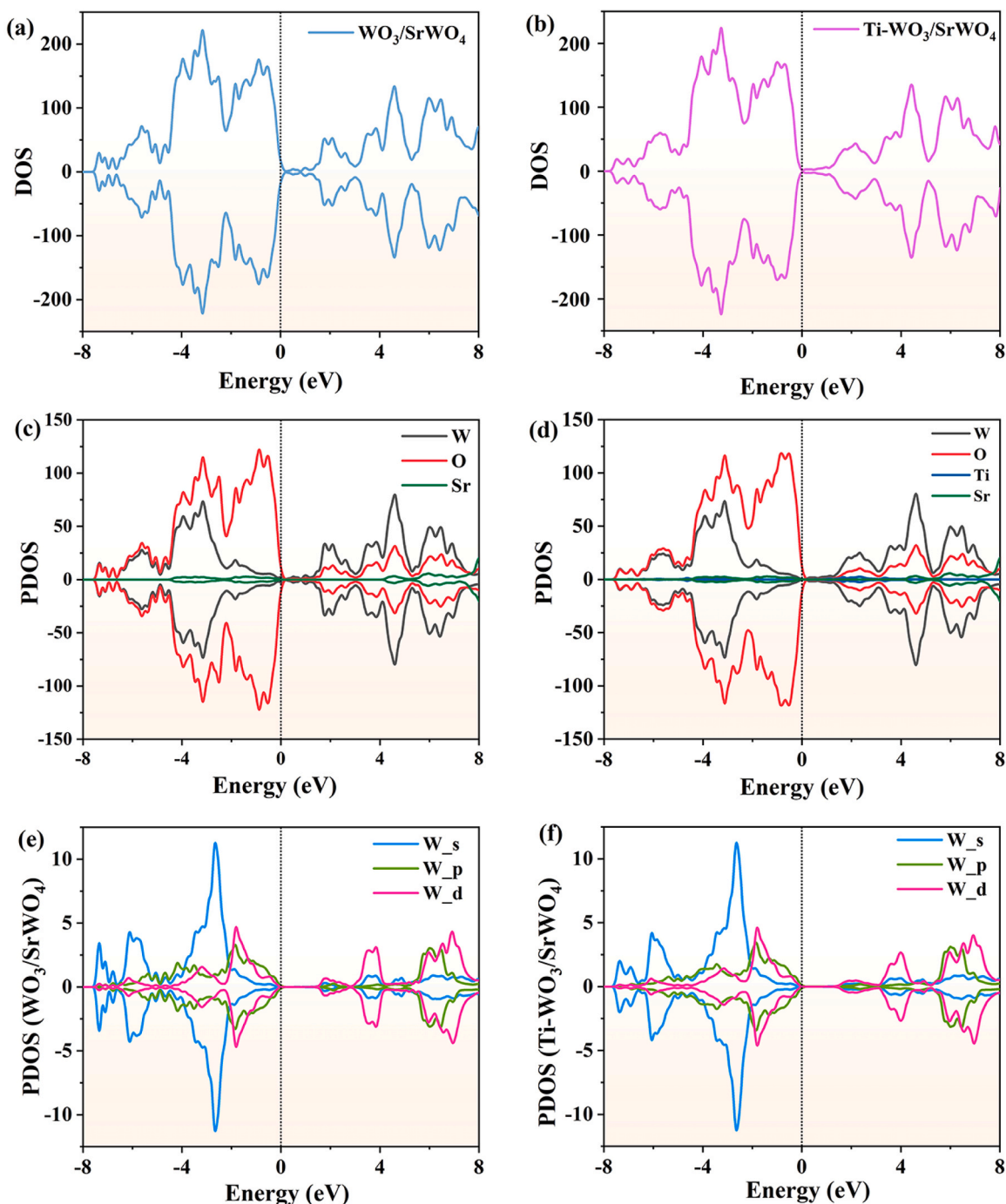
Fig. 8. DOS and PDOS of WO$_3$/SrWO$_4$ (a-c) and Ti-WO$_3$/SrWO$_4$ (e-f).

reactions continue, resulting in a stable state 3. In the last step, the hydrogenation reaction generates two NH$_3$ molecules, and Ti^{4+} is reduced to Ti^{3+} simultaneously. This cycle is repeated until a large amount of NH$_3$ is produced.

4. Conclusion

In this study, Ti–WO$_3$/SrWO$_4$ was prepared by simple hydrothermal and spin-coating methods. The heterojunction formed by WO$_3$ and SrWO$_4$ inhibited the complexation of photogenerated carriers. Ti, as a nitrogen adsorption site, promoted nitrogen activation, thereby improving the carrier transport efficiency and NH$_3$ synthesis performance. Ti–WO$_3$/SrWO$_4$ was more sensitive to N$_2$ and had excellent NRR

performance; this combination, therefore, provides a new idea for regulating the catalyst surface interface for the PEC synthesis of NH$_3$.

CRediT authorship contribution statement

Kaiyi Chen: Conceptualization, Methodology, Investigation, Formal analysis, Writing – original draft, Writing. **Xiaohong Xu:** Experiments, Writing – origin draft. **Qiong Mei:** Data curation. **Jingwei Huang:** Writing – review & editing. **Guidong Yang:** Writing – review & editing. **Qizhao Wang:** Conceptualization, Supervision, Writing – review & editing.
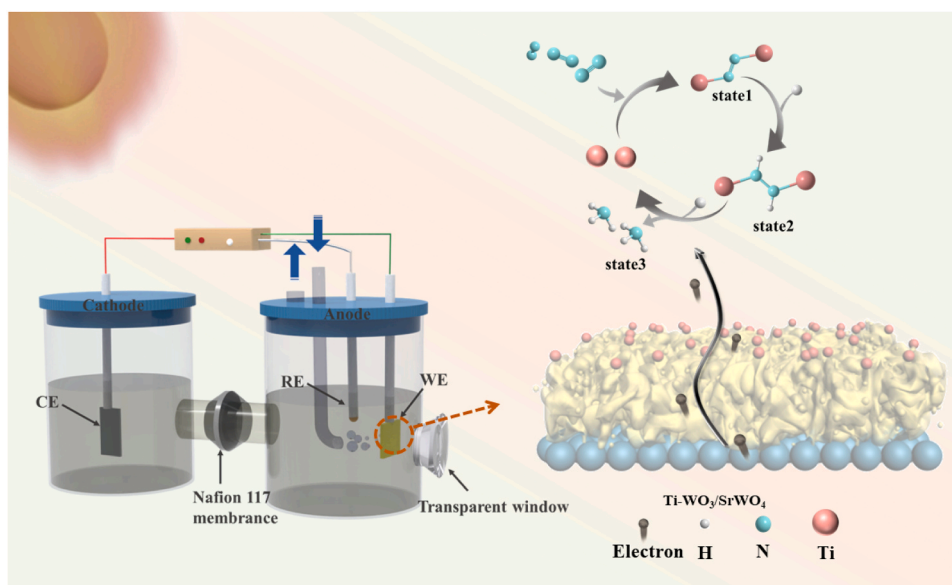
Fig. 9. Mechanism diagram of synthetic ammonia.

Declaration of Competing Interest

All authors declared that they do not have any commercial or associative interest that represents a conflict of interest in connection with the work submitted.

Data Availability

Data will be made available on request.

Acknowledgements

Appendix A. Supporting information

Supplementary data associated with this article can be found in the online version at doi:10.1016/j.apcatb.2023.123299.

References

[1] T. Oshikiri, K. Ueno, H. Misawa, Selective dinitrogen conversion to ammonia using water and visible light through plasmon-induced charge separation, Angew. Chem. Int. Ed. 55 (2016) 3942–3946, https://doi.org/10.1002/anie.201511189.

[2] Y. Zhao, Y. Zhao, G.I.N. Waterhouse, L. Zheng, X. Cao, F. Teng, L.-Z. Wu, C.-H. Tung, D. O'Hare, T. Zhang, Layered-double-hydroxide nanosheets as efficient visible-light-driven photocatalysts for dinitrogen fixation, Adv. Mater. 29 (2017), 1703828, https://doi.org/10.1002/adma.201703828.

[3] S. Hu, Y. Li, F. Li, Z. Fan, H. Ma, W. Li, X. Kang, Construction of g-C$_3$N$_4$/Zn$_{0.11}$Sn$_{0.12}$Cd$_{0.88}$S$_{1.12}$ hybrid heterojunction catalyst with outstanding nitrogen photofixation performance induced by sulfur vacancies, ACS Sustain. Chem. Eng. 4 (2016) 2269–2278, https://doi.org/10.1021/acssuschemeng.5b01742.

[4] S. Wang, L. Zhang, Z. Xia, A. Roy, D.W. Chang, J.-B. Baek, L. Dai, BCN graphene as efficient metal-free electrocatalyst for the oxygen reduction reaction, Angew. Chem., Int. Ed. 51 (2012) 4209–4212, https://doi.org/10.1002/anie.201109257.

[5] H. Zeng, L. Liu, D. Zhang, Y. Wang, Z. Li, C. Liu, L. Zhang, X. Cui, Fe (III)-C$_3$N$_4$ hybrids photocatalyst for efficient visible-light driven nitrogen fixation, Mater. Chem. Phys. 258 (2021), 123830, https://doi.org/10.1016/j.matchemphys.2020.123830.

[6] M. Arif, G. Yasin, L. Luo, W. Ye, M.A. Mushtaq, X. Fang, X. Xiang, S. Ji, D. Yan, Hierarchical hollow nanotubes of NiFeV-layered double hydroxides@ CoVP heterostructures towards efficient, pH-universal electrocatalytical nitrogen reduction reaction to ammonia, Appl. Catal. B 265 (2020), 118559, https://doi.org/10.1016/j.apcatb.2019.118559.

[7] J. Xu, T.J.K. Brenner, L. Chabanne, D. Neher, M. Antonietti, M. Shalom, Liquid-based growth of polymeric carbon nitride layers and their use in a mesostructured polymer solar cell with Voc exceeding 1 V, J. Am. Chem. Soc. 136 (2014) 13486–13489, https://doi.org/10.1021/ja508329c.

[8] Y. Li, Q. Wang, X. Hu, Y. Meng, H. She, L. Wang, J. Huang, G. Zhu, Constructing NiFe-metal-organic frameworks from NiFe-layered double hydroxide as a highly efficient cocatalyst for BiVO$_4$ photoanode PEC water splitting, Chem. Eng. J. 433 (2022), 133592, https://doi.org/10.1016/j.cej.2021.133592.

[9] S. Mansingh, K.K. Das, A. Behera, S. Subudhi, S. Sultana, K. Parida, Bandgap engineering via boron and sulphur doped carbon modified anatase TiO$_2$: a visible light stimulated photocatalyst for photo-fixation of N$_2$ and TCH degradation, Nanoscale Adv. 2 (2020) 2004–2017, https://doi.org/10.1039/D0NA00183J.

[10] J. Wang, C. Hua, X. Dong, Y. Wang, N. Zheng, Synthesis of plasmonic bismuth metal deposited InVO$_4$ nanosheets for enhancing solar light-driven photocatalytic nitrogen fixation, Sustain. Energy Fuels 4 (2020) 1855–1862, https://doi.org/10.1039/C9SE01136F.

[11] Y. Lu, B. Ma, Y. Yang, E. Huang, Z. Ge, T. Zhang, S. Zhang, L. Li, N. Guan, Y. Ma, Y. Chen, High activity of hot electrons from bulk 3D graphene materials for efficient photocatalytic hydrogen production, Nano Res. 10 (2017) 1662–1672, https://doi.org/10.1007/s12274-016-1390-5.

[12] X. Li, W. Fan, D. Xu, J. Ding, H. Bai, W. Shi, Boosted photoelectrochemical N$_2$ reduction over Mo$_2$C in situ coated with graphitized carbon, Langmuir 36 (2020) 14802–14810, https://doi.org/10.1021/acs.langmuir.0c02770.

[13] M. Ali, F. Zhou, K. Chen, C. Kotzur, C. Xiao, L. Bourgeois, X. Zhang, D. R. MacFarlane, Nanostructured photoelectrochemical solar cell for nitrogen reduction using plasmon-enhanced black silicon, Nat. Commun. 7 (1) (2016) 5, https://doi.org/10.1038/ncomms11335.

[14] Q. Su, W. Wang, Z. Zhang, J. Duan, Enhanced photocatalytic performance of Cu$_2$O/MoS$_2$/ZnO composites on Cu mesh substrate for nitrogen reduction, Nanotechnol 32 (2021), 285706, https://doi.org/10.1088/1361-6528/abf378.

[15] Q. Zhang, S. Hu, Z. Fan, D. Liu, Y. Zhao, H. Ma, F. Li, Preparation of g-C$_3$N$_4$/ZnMoCdS hybrid heterojunction catalyst with outstanding nitrogen photofixation performance under visible light via hydrothermal post-treatment, Dalton Trans. 45 (2016) 3497–3505, https://doi.org/10.1039/C5DT04901F.

[16] X. Xue, R. Chen, C. Yan, Y. Hu, W. Zhang, S. Yang, L. Ma, G. Zhu, Z. Jin, Efficient photocatalytic nitrogen fixation under ambient conditions enabled by the heterojunctions of n-type Bi$_2$MoO$_6$ and oxygen-vacancy-rich p-type BiOBr, Nanoscale 11 (2019) 10439–10445, https://doi.org/10.1039/C9NR02279A.

[17] H. Liang, H. Zou, S. Hu, Preparation of the W$_{18}$O$_{49}$/g-C$_3$N$_4$ heterojunction catalyst with full-spectrum-driven photocatalytic N$_2$ photofixation ability from the UV to near infrared region, New J. Chem. 41 (2017) 8920–8926, https://doi.org/10.1039/C7NJ01848G.

[18] F. Xu, J. Zhang, B. Zhu, J. Yu, J. Xu, CuInS$_2$ sensitized TiO$_2$ hybrid nanofibers for improved photocatalytic CO$_2$ reduction, Appl. Catal., B 230 (2018) 194–202, https://doi.org/10.1016/j.apcatb.2018.02.042.

[19] A. Kumar, A. Kumar, G. Sharma, Aa.H. Al-Muhtaseb, M. Naushad, A.A. Ghfar, C. Guo, F.J. Stadler, Biochar-templated g-C$_3$N$_4$/Bi$_2$O$_2$CO$_3$/CoFe$_2$O$_4$ nano-assembly for visible and solar assisted photo-degradation of paraquat, nitrophenol reduction and CO$_2$ conversion, Chem. Eng. J. 339 (2018) 393–410, https://doi.org/10.1016/j.cej.2018.01.105.

[20] X. Rong, S. Liu, M. Xie, Z. Liu, Z. Wu, X. Zhou, X. Qiu, J. Wei, N_2 photofixation by Z-scheme single-layer g-C_3N_4/$ZnFe_2O_4$ for cleaner ammonia production, Mater. Res. Bull. 127 (2020), 110853, https://doi.org/10.1016/j.materresbull.2020.110853.

[21] Y. Li, M. Ti, D. Zhao, Y. Zhang, L. Wu, Y. He, Facile synthesis of nitrogen-vacancy pothole-rich few-layer g-C_3N_4 for photocatalytic nitrogen fixation into nitrate and ammonia, J. Alloy. Compd. 870 (2021), 159298, https://doi.org/10.1016/j.jallcom.2021.159298.

[22] R. Zheng, C. Li, K. Huang, Y. Guan, B. Sun, W. Wang, L. Wang, J. Bian, TiO_2/Ti_3C_2 intercalated with g-C_3N_4 nanosheets as 3D/2D ternary heterojunctions photocatalyst for the enhanced photocatalytic reduction of nitrate with high N_2 selectivity in aqueous solution, Inorg. Chem. Front. 8 (2021) 2518–2531, https://doi.org/10.1039/D1QI00001B.

[23] L. Shi, Z. Li, L. Ju, A. Carrasco-Pena, N. Orlovskaya, H. Zhou, Y. Yang, Promoting nitrogen photofixation over a periodic WS_2@TiO_2 nanoporous film, J. Mater. Chem. A 8 (2020) 1059–1065, https://doi.org/10.1039/C9TA12743G.

[24] X. Yu, H. Qiu, Z. Wang, B. Wang, Q. Meng, S. Sun, Y. Tang, K. Zhao, Constructing the Z-scheme TiO_2/Au/BiOI nanocomposite for enhanced photocatalytic nitrogen fixation, Appl. Surf. Sci. 556 (2021), 149785, https://doi.org/10.1016/j.apsusc.2021.149785.

[25] F. Xu, B. Zhu, B. Cheng, J. Yu, J. Xu, 1D/2D TiO_2/MoS_2 hybrid nanostructures for enhanced photocatalytic CO_2 reduction, Adv. Opt. Mater. 6 (2018), 1800911, https://doi.org/10.1002/adom.201800911.

[26] J. Tang, Y. Liu, Y. Lin, X. Liu, L. Chen, C. Piao, D. Fang, J. Wang, Design and construction of diverse dual co-catalysts decorated Z-scheme g-C_3N_4/WO_3(002) photocatalyst for converting nitrate and sulfite, Opt. Mater. 121 (2021), 111541, https://doi.org/10.1016/j.optmat.2021.111541.

[27] S. Zhou, C. Zhang, J. Liu, J. Liao, Y. Kong, Y. Xu, G. Chen, Formation of an oriented Bi_2WO_6 photocatalyst induced by in situ Bi reduction and its use for efficient nitrogen fixation, Catal. Sci. Technol. 9 (2019) 5562–5566, https://doi.org/10.1039/C9CY00972H.

[28] Y. Du, C. Jiang, L. Song, B. Gao, H. Gong, W. Xia, L. Sheng, T. Wang, J. He, Regulating surface state of WO_3 nanosheets by gamma irradiation for suppressing hydrogen evolution reaction in electrochemical N_2 fixation, Nano Res 13 (2020) 2784–2790, https://doi.org/10.1007/s12274-020-2929-z.

[29] L. Bao, Y.-j Yuan, H. Zhang, X. Zhang, G. Xu, Understanding the hierarchical behavior of Bi_2WO_6 with enhanced photocatalytic nitrogen fixation activity, Dalton Trans. 50 (2021) 7427–7432, https://doi.org/10.1039/D1DT00762A.

[30] Y. Cao, S. Hu, F. Li, Z. Fan, J. Bai, G. Lu, Q. Wang, Photofixation of atmospheric nitrogen to ammonia with a novel ternary metal sulfide catalyst under visible light, RSC Adv. 6 (2016) 49862–49867, https://doi.org/10.1039/C6RA08247E.

[31] J. Zheng, L. Lu, K. Lebedev, S. Wu, P. Zhao, I.J. McPherson, T.-S. Wu, R. Kato, Y. Li, P.-L. Ho, G. Li, L. Bai, J. Sun, D. Prabhakaran, R.A. Taylor, Y.-L. Soo, K. Suenaga, S.C.E. Tsang, Fe on molecular-layer MoS_2 as inorganic Fe-S_2-Mo motifs for light-driven nitrogen fixation to ammonia at elevated temperatures, Chem. Catal. 1 (2021) 162–182, https://doi.org/10.1016/j.checat.2021.03.002.

[32] J. Zhang, X. Tian, M. Liu, H. Guo, J. Zhou, Q. Fang, Z. Liu, Q. Wu, J. Lou, Cobalt-modulated molybdenum–dinitrogen interaction in MoS_2 for catalyzing ammonia

synthesis, J. Am. Chem. Soc. 141 (2019) 19269–19275, https://doi.org/10.1021/jacs.9b02501.

[33] Q. Li, X. Bai, J. Luo, C. Li, Z. Wang, W. Wu, Y. Liang, Z. Zhao, Fe doped $SrWO_4$ with tunable band structure for photocatalytic nitrogen fixation, Nanotechnol 31 (2020) 375402,. 10.1088/1361-6528/ab9863..

[34] H. Zhang, Y. Chen, Y. Pan, L. Bao, Y.-J. Yuan, Hydrogen pressure-assisted rapid recombination of oxygen vacancies in WO_3 nanosheets for enhanced N_2 photofixation, J. Solid State Chem. 303 (2021), 122520, https://doi.org/10.1016/j.jssc.2021.122520.

[35] Z. Sun, R. Huo, C. Choi, S. Hong, T.-S. Wu, J. Qiu, C. Yan, Z. Han, Y. Liu, Y.-L. Soo, Oxygen vacancy enables electrochemical N_2 fixation over WO_3 with tailored structure, Nano Energy 62 (2019) 869–875, https://doi.org/10.1016/j.nanoen.2019.06.019.

[36] G. Kresse, J. Furthmüller, Efficiency of ab-initio total energy calculations for metals and semiconductors using a plane-wave basis set, Comput. Mater. Sci. 6 (1996) 15–50, https://doi.org/10.1016/0927-0256(96)00008-0.

[37] G. Kresse, J. Furthmüller, Efficient iterative schemes for ab initio total-energy calculations using a plane-wave basis set, Matter Mater. Phys. 54 (1996) 11169, https://doi.org/10.1103/PhysRevB.54.11169.

[38] J.P. Perdew, K. Burke, M. Ernzerhof, Generalized gradient approximation made simple, Phys. Rev. Lett. 77 (1996) 3865, https://doi.org/10.1103/PhysRevLett.77.3865.

[39] S. Grimme, Semiempirical GGA-type density functional constructed with a long-range dispersion correction, Comput. Chem. 27 (2006) 1787–1799, https://doi.org/10.1002/jcc.20495.

[40] V. Wang, N. Xu, J. Liu, G. Tang, W. Geng, VASPKIT: A user-friendly interface facilitating high-throughput computing and analysis using VASP code, Comput. Phys. Commun. 267 (2021), 108033, https://doi.org/10.1016/j.cpc.2021.108033.

[41] X. Hu, Q. Wang, Y. Li, Y. Meng, L. Wang, H. She, J. Huang, The hydrophilic treatment of a novel co-catalyst for greatly improving the solar water splitting performance over Mo-doped bismuth vanadate, Science 607 (2022) 219–228, https://doi.org/10.1016/j.jcis.2021.08.195.

[42] Y. Li, Q. Mei, Z. Liu, X. Hu, Z. Zhou, J. Huang, B. Bai, H. Liu, F. Ding, Q. Wang, Fluorine-doped iron oxyhydroxide cocatalyst: promotion on the WO_3 photoanode conducted photoelectrochemical water splitting, J. Colloid Interface Sci. 304 (2022), 120995, https://doi.org/10.1016/j.apcatb.2021.120995.

[43] S.M. M Zawawi, R. Yahya, A. Hassan, H.N.M.E. Mahmud, M.N. Daud, Structural and optical characterization of metal tungstates (MWO_4; M=Ni, Ba, Bi) synthesized by a sucrose-templated method, Chem. Cent. J. 7 (2013), 80, https://doi.org/10.1186/1752-153X-7-80.

[44] P. Nehra, A. Khatri, A. Kumar, S. Singh, P. Rana, Synthesis and characterization of rare earth metal doped tungsten trioxide photocatalyst for degradation of Rhodamine B dye, J. Rare Earth 41 (2023) 1302–1310, https://doi.org/10.1016/j.jre.2022.07.007.

[45] C.C. McCrory, S. Jung, J.C. Peters, T.F. Jaramillo, Benchmarking heterogeneous electrocatalysts for the oxygen evolution reaction, J. Am. Chem. Soc. 135 (2013) 16977–16987, https://doi.org/10.1021/ja407115p.